

## RESEARCH ARTICLE

Electrospun Mo—SiO<sub>2</sub> nanofibers as heterogeneous catalysts for propylene metathesis

Tomas Pokorny<sup>1</sup>  | Ran Zhu<sup>2</sup>  | Lucie Simonikova<sup>1</sup>  | Ales Styskalik<sup>1</sup>  | Yuriy Román-Leshkov<sup>2</sup>  | David Skoda<sup>3</sup> 

<sup>1</sup>Department of Chemistry, Masaryk University, Brno, Czech Republic

<sup>2</sup>Department of Chemical Engineering, Massachusetts Institute of Technology (MIT), Cambridge, Massachusetts, USA

<sup>3</sup>Center of Polymer Systems, Tomas Bata University in Zlín, Zlín, Czech Republic

## Correspondence

Ales Styskalik, Department of Chemistry, Masaryk University, Brno, Czech Republic.

Email: [styskalik@chemi.muni.cz](mailto:styskalik@chemi.muni.cz)

Yuriy Román-Leshkov, Department of Chemical Engineering, Massachusetts Institute of Technology (MIT), Cambridge, Massachusetts, USA.  
Email: [yroman@mit.edu](mailto:yroman@mit.edu)

David Skoda, Center of Polymer Systems, Tomas Bata University in Zlín, Zlín, Czech Republic.  
Email: [dskoda@utb.cz](mailto:dskoda@utb.cz)

## Funding information

Ministry of Education, Youth, and Sports of the Czech Republic, Grant/Award Numbers: LUAUS23085, LM2023042, LM2023051, CZ.02.01.01/00/22\_008/0004572; European Regional Development Fund-Project “UP CHSB”, Grant/Award Number: CZ.02.1.01/0.0/0.0/18\_046/0015974

## Abstract

Olefin metathesis catalysts based on molybdenum exhibit superior performance at low temperatures when they contain highly dispersed MoO<sub>x</sub> species within the catalyst support. However, the preparation methods that achieve this high dispersion are often difficult to scale up. In this study, we report the scalable synthesis of molybdenum silicate (Mo—SiO<sub>2</sub>) nanofibers (NFs) via electrospinning, aimed at producing catalysts active in olefin metathesis reactions. The resulting NFs had diameters ranging from 70 to 209 nm and exhibited high surface areas, reaching up to 920 m<sup>2</sup> g<sup>−1</sup>. A comprehensive characterization of the MoO<sub>x</sub> active sites—using powder x-ray diffraction analysis, Raman spectroscopy, x-ray photoelectron spectroscopy, HRTEM, H<sub>2</sub>-TPR, and in situ DRUV-Vis—confirmed the absence of crystalline phases, indicating a high degree of dispersion and uniformity. Among the prepared samples, Mo—SiO<sub>2</sub> containing 5 wt% Mo, with an average fiber diameter of 104 nm and a surface area of 456 m<sup>2</sup> g<sup>−1</sup>, demonstrated exceptional catalytic performance in propylene self-metathesis. It achieved a propylene metathesis rate of 17.1 μmol g<sup>−1</sup> s<sup>−1</sup> at 200°C, significantly outperforming a catalyst prepared via incipient wetness impregnation, used here as a model for industrial benchmarks.

## KEYWORDS

catalysts/catalysis, electrospinning, molybdenum silicates, nanostructures, olefin metathesis, porous materials

## 1 | INTRODUCTION

Olefin metathesis is an essential catalytic reaction for rearranging C=C bonds in olefins,<sup>1</sup> with broad applications

in organic<sup>2</sup> and polymer chemistry,<sup>3</sup> pharmaceuticals,<sup>4</sup> or biochemistry.<sup>5</sup> It has become an indispensable synthetic tool, particularly as the increasing demand for propylene drives significant advancements in catalyst technologies.

This is an open access article under the terms of the [Creative Commons Attribution](https://creativecommons.org/licenses/by/4.0/) License, which permits use, distribution and reproduction in any medium, provided the original work is properly cited.

© 2025 The Author(s). *Journal of the American Ceramic Society* published by Wiley Periodicals LLC on behalf of American Ceramic Society.

Traditionally, silica-supported tungsten oxides catalysts<sup>6</sup> have been used for cross-metathesis of ethylene and 2-butenes in the Phillips triolefin process, typically requiring temperatures above 300°C.<sup>7–9</sup> To overcome these limitations, recent efforts have focused on non-rare earth metal molybdenum-based catalysts.

Supported molybdenum oxides, with supports such as SiO<sub>2</sub>,<sup>10–12</sup> Al<sub>2</sub>O<sub>3</sub>,<sup>13</sup> mixed oxide SiO<sub>2</sub>–Al<sub>2</sub>O<sub>3</sub>,<sup>13–15</sup> SiO<sub>2</sub> doped with main group elements or transition metals,<sup>7,16</sup> and zeolites,<sup>13,17</sup> could offer higher activity under milder conditions and hold promise for long-term industrial applications.<sup>18</sup> The mechanism of olefin metathesis over molybdenum-based heterogeneous catalysts remains incompletely understood,<sup>19,20</sup> with the coordination, the oxidation state, and connectivity of single Mo sites still under debates.<sup>19,20</sup> Nevertheless, an atomically dispersed Mo-dioxo structure is widely proposed as the pre-active site, which undergoes in situ transformation into an Mo-oxo alkylidene structure during olefin metathesis.<sup>14,21</sup>

The scalable incipient wetness impregnation (IWI) method is commonly used to deposit MoO<sub>x</sub> on silica and other supports.<sup>20</sup> This approach typically results in relatively random Mo dispersion, with MoO<sub>x</sub> sites beginning to oligomerize above a certain surface density.<sup>14</sup> To address this, various synthetic strategies, including flame spray pyrolysis,<sup>21</sup> advanced sol–gel techniques,<sup>22–27</sup> surface organometallic chemistry (SOMC),<sup>19,28,29</sup> and anion exchange,<sup>30</sup> have been developed to achieve greater control over active site structure. Particularly, Skoda and Zhu recently achieved high MoO<sub>x</sub> dispersion in silica with up to 11 wt% Mo content using a microwave-assisted sol–gel method, producing microspherical catalysts.<sup>22,25</sup> These samples showed superior catalytic activity compared to the traditional IWI-prepared samples under identical reaction conditions.<sup>25,26,31–33</sup> Although tailored MoO<sub>x</sub> dispersion represents the primary advantage of these advanced synthetic methods, scaling them up for industrial application remains a significant challenge.

Electrospinning has emerged as a versatile and scalable method for fabricating nanofibers (NFs).<sup>34</sup> This process involves applying a high voltage to an electrospun solution, typically of a polymer, or melt, resulting in the formation of a jet that solidifies into NFs. The electrospinning technique enables precise control over NF diameter,<sup>35,36</sup> composition,<sup>37,38</sup> and morphology,<sup>39–41</sup> allowing for tailored designs suited to specific catalytic applications.<sup>42,43</sup> NFs offer distinct advantages similar to other nanostructures, including increased surface area, enhanced porosity, and superior mass transfer properties, all of which can contribute to improved catalytic performance.<sup>44</sup>

A key challenge lies in achieving well-dispersed MoO<sub>x</sub> species within silica NFs to enable the in situ formation of active metal–carbene sites that drive the Chauvin cycle.<sup>19,20,31</sup> The presented study addresses this challenge

by combining the advantages of electrospinning and sol–gel synthesis to establish a scalable and continuous process for preparation of silica-based NFs with highly dispersed MoO<sub>x</sub> active centers. The outstanding catalytic performance of Mo–SiO<sub>2</sub> NFs is demonstrated in propylene self-metathesis catalytic reaction.

## 2 | METHODS

### 2.1 | Materials

Bis(acetylacetonato)dioxomolybdenum(VI) (MoO<sub>2</sub>(Acac)<sub>2</sub>) (99%, Merck) was used as a molybdenum precursor in all reactions. Dimethylformamide (DMF) (99.5%, Penta), tetraethyl orthosilicate (TEOS) (99%, Merck), polyvinylpyrrolidone (PVP) (average molecular weight: 360 000 g mol<sup>−1</sup>, Merck), and HCl (35%, Lachner) were used without additional purification and used for nanofibers preparation.

Propylene (99.5%, Airgas), helium (99.999%, UHP, Airgas) used in the catalytic test were further purified using in-house built traps consisting of molecular sieves (3 Å, Sigma-Aldrich) and supported Cu samples (BASF R3-11G, Research Catalysts Inc.). House air was used after sequentially purification using a Wilkerson modular compressed air filter (McMaster-Carr), an FID tower (NM Plus 1350 FID tower, VICI DBS), and an indicating moisture trap (Restek).

### 2.2 | Synthesis

The solution for the synthesis of Mo–SiO<sub>2</sub> NFs was prepared as follows: PVP (1.2 g) and the desired amount of MoO<sub>2</sub>(Acac)<sub>2</sub> were dissolved in 9.0 g of DMF, and stirred at 70°C until the transparent solution was formed. Then, the solution was cooled to room temperature, and TEOS (2.5 g) was added dropwise to a rapidly stirred polymer solution. After a clear solution was formed, its conductivity was adjusted to 1.0 mS cm<sup>−1</sup> by the dropwise addition of concentrated HCl (35%). The electrical conductivity of the solutions was set with the help of an XS Instrument Cond51 conductometer.

The benchmark catalysts were prepared by IWI. Full synthetic procedure as well as characterization can be found elsewhere.<sup>25,45</sup>

### 2.3 | Electrospinning

A small lab-scale setup was used for the electrospinning process (Figure S1). The prepared solution was loaded into a syringe with a metal needle (1.0 mm diameter). A syringe

pump was maintained at the flow rate of  $1.5 \mu\text{L min}^{-1}$  to prevent dripping and minimize splashing to produce a uniform layer of NFs on the collector. The distance from the needle tip to a collector was 15.0 cm, 16 kV of voltage was applied, +8 kV was applied to the needle, and −8 kV to the collector. The drum collector (diameter 10 cm) covered with aluminum foil was rotating slowly at around 10 rpm. Prepared green NFs were calcined in a muffle furnace under static air using a heating rate of  $3^\circ\text{C min}^{-1}$  to  $500^\circ\text{C}$  for 3 h (according to thermogravimetry [TG] analysis Figure S2).

## 2.4 | Characterization

The MiniFlex 600 instrument by Rigaku was used to measure powder x-ray diffraction analysis (PXRD). The  $\text{Co } K_\alpha$  radiation ( $\lambda = 1.7903 \text{ \AA}$ ) was used (15 mA, 40 kV). Data processing was performed with Rigaku PDXL2 software.

TG was measured on device STA 449 by NETZCH. Samples were measured in a platinum crucible with air set to  $100 \text{ cm}^3 \text{ min}^{-1}$ , the heating rate was  $5^\circ\text{C min}^{-1}$ , and samples were heated up to  $1000^\circ\text{C}$ .

The elemental experimental composition of samples was determined by inductively coupled plasma optical emission spectroscopy (ICP-OES). Samples were mineralized with a 1:1 ratio of  $\text{HF}:\text{HNO}_3$ . Measurements were done on the iCAP PRO x-ray photoelectron spectroscopy (XPS) instrument (Thermo, RF Power 1.10 kW, nebulizer gas flow  $0.65 \text{ dm}^3 \text{ min}^{-1}$ , and radial viewing height 11.0 mm).

XPS and Kratos Axis Supra instrument measured surface composition NFs. The instrument was equipped with a monochromatic x-ray source with  $\text{Al } K_\alpha$  ( $E = 1486.6 \text{ eV}$ ) excitation and  $\text{Si } 2p$  in  $\text{SiO}_2$  (binding energy 103.3 eV) was used as a calibration reference.

Raman spectra were recorded under ambient atmospheric conditions using a DXR Raman Microscope (Thermo Fisher Scientific) equipped with a 780-nm wavelength laser. The laser power was set to 20 mW, and spectra were collected in the range of  $50\text{--}2000 \text{ cm}^{-1}$ . A high-resolution grating was employed during the measurements.

The specific surface area (SSA) was determined through nitrogen porosimetry utilizing an Autosorb iQ3 instrument by Quantachrome Instruments. Measurements were conducted at a temperature of 77 K to obtain adsorption and desorption isotherms. Prior to measurements, samples underwent degassing for a minimum of 12 h at  $200^\circ\text{C}$ . The BET analysis provided SSA values from observed isotherms throughout a relative pressure range of 0.05–0.30. The micropore analysis was performed using the  $t$ -method. Argon porosimetry was performed on same device with temperature 87 K using Cryosync attachment.

For the scanning electron microscopy (SEM) analysis, a Versa 3D instrument manufactured by the Thermo Fisher Scientific company was used. Scanning was performed in a single or double lens mode using backscattered electrons or secondary electrons detection. The diameter of fibers and distribution data were obtained using the ImageJ software analyzing at least 100 fibers from one micrograph per sample.<sup>46</sup>

For the HRTEM and STEM analysis, the samples were dispersed by ultrasonication in hexane and drop-casted onto a copper grid with a lacey carbon film. EDS was measured on a Thermo Scientific Talos F200i equipped with a Bruker Dual-X spectrometer, operated in the STEM regime at a high voltage of 200 kV and beam current of 0.5 nA. Spectrum images were post-processed using the Velox software. Micrographs were analyzed using the ImageJ program to determine the object's diameters.

The reducibility of  $\text{Mo--SiO}_2$  NFs was studied by hydrogen temperature-programmed reduction ( $\text{H}_2$ -TPR). Measurements were conducted on a Micrometric Autochem II 2920 system equipped with a thermal conductivity detector. Approximately 50 mg of ground NFs were loaded in a U-shape quartz reactor between layers of quartz wool. The sample pretreatment involved heating to  $400^\circ\text{C}$  under a  $50\text{-mL min}^{-1}$  flow of 5%  $\text{O}_2$  in He at a heating rate of  $3^\circ\text{C min}^{-1}$  for 3 h, followed by purging at  $150^\circ\text{C}$  under a  $50\text{-mL min}^{-1}$  flow of He for 1 h.  $\text{H}_2$ -TPR analysis was performed under a  $50\text{-mL min}^{-1}$  flow of 10%  $\text{H}_2$  in He, with temperature ramped from 100 to  $900^\circ\text{C}$  at a heating range of  $10^\circ\text{C min}^{-1}$ .

In situ DRUV-Vis spectrometry was performed using a Cary 5000 UV-Vis-NIR spectrophotometer equipped with a diffusion IR environmental chamber (162–4200, PIKE technologies).  $\text{BaSO}_4$  (99 wt%, Millipore Sigma) under ambient conditions served as the baseline material for all measurements. Prior to each measurement, samples were pretreated by heating to  $400^\circ\text{C}$  under a  $60\text{-mL min}^{-1}$  flow of purified air at a heating rate of  $3^\circ\text{C min}^{-1}$  for 3 h, followed by cooling to room temperature under the same flow of purified air. Diffuse reflectance measurements were initially converted to absorbance using the Kubelka–Munk function. The edge energy for direct allowed transitions was determined from the intercept of a straight line fitted to the low-energy onset in the plot of  $[\text{FR}(\infty)/h\nu]^2$  versus  $h\nu$  (incident photon energy).

## 2.5 | Catalytic experiments

The catalytic performance of the  $\text{Mo--SiO}_2$  NFs was evaluated using a packed-bed reactor, as described in detail elsewhere.<sup>25</sup> In a typically experiment, approximately 10 mg of NFs was ground into fine particles and mixed

**TABLE 1** Nominal and experimental (inductively coupled plasma optical emission spectroscopy [ICP-OES]) Mo loading in Mo–SiO<sub>2</sub> nanofibers and their average diameters (scanning electron microscopy [SEM]).

Sample	Nominal Mo (wt%)	Experimental Si:Mo ratio (ICP-OES)	Mo (wt%) (ICP-OES) <sup>a</sup>	Nanofibers average diameter (nm)	Diameter distribution (nm) <sup>b</sup>
2Mo–SiO <sub>2</sub>	2	1:75.2	2.06	184	42
5Mo–SiO <sub>2</sub>	5	1:28.1	5.29	100	27
7Mo–SiO <sub>2</sub>	7	1:20.7	6.99	79	24
11Mo–SiO <sub>2</sub>	11	1:13.7	10.22	113	23

<sup>a</sup>Mo wt% calculated from experimental Mo:Si and assumption of MoO<sub>3</sub>SiO<sub>2</sub> structure.<sup>b</sup>Calculated by standard deviation.

with 100 mg of silicon carbide (SiC). The catalyst bed was packed between two layers of inert SiC (150 mg each) and secured with quartz wool plugs (4–6  $\mu\text{m}$ , Technical Glass Products). The reaction temperature was monitored using an upstream type-K thermocouple (Omega Engineering). The packed bed was pretreated by heating to 400°C at a heating rate of 3°C min<sup>−1</sup> for 3 h, followed by cooling to 300°C under a 60 mL min<sup>−1</sup> flow of purified air. The sample was then purged for 30 min and activated at 500°C (2°C min<sup>−1</sup>) for 3 h under a 100-mL min<sup>−1</sup> flow of He. Finally, the sample was cooled to the reaction temperature and exposed to a mixture of propylene and He at the desired propylene concentration. The reactor effluent was analyzed by online gas chromatography (GC; Shimadzu GC-2014) equipped with an Agilent HP-PLOT Al<sub>2</sub>O<sub>3</sub>-S (30 m  $\times$  0.25 mm) column and a flame ionization detector. In this study, all reported rates refer to the propylene metathesis rate, defined as the sum of the production rates of ethylene, *trans*-2-butene, and *cis*-2-butene.

### 3 | RESULTS AND DISCUSSION

In this study, we developed the preparation of NFs containing molybdenum embedded in the silica matrices (Mo–SiO<sub>2</sub>). Elemental composition of the prepared NFs was analyzed using the ICP-OES method (Table 1). The experimental results for Mo content aligned with the prepared solutions' nominal values, demonstrating the electrospinning method's effectiveness in precisely controlling the final Mo content across the range of 2–10 wt%. The ability to accurately control the Mo content further highlights the versatility and reliability of this preparation method, enabling the tailoring of NF properties for specific applications, such as heterogeneous catalysis.

SEM analysis of the calcined Mo–SiO<sub>2</sub> NFs revealed smooth, uniform, and round fibers (Figure 1). All samples demonstrated high uniformity with minimal inhomogeneities, such as beads and plates. However, the 5Mo–SiO<sub>2</sub> and 7Mo–SiO<sub>2</sub> samples exhibited slightly reduced homogeneity, likely caused by dispersed droplets

during the spinning process, as shown in Figure S3. The Mo content influenced the final diameter of the NFs, though no clear trend was observed. The average diameter of all calcined Mo–SiO<sub>2</sub> NFs ranged from 70 to 200 nm (Table 1), and a histogram of NFs' diameters is shown in Figure S4. Notably, the 5Mo–SiO<sub>2</sub> and 7Mo–SiO<sub>2</sub> NFs had an average diameter of 104 and 70 nm, respectively, highlighting the readily achievable nanometer-range fibers with this synthesis procedure compared to the methods described in the literature.<sup>47–49</sup>

STEM analysis revealed that the prepared NFs exhibit uniform fibrous structure (Figure 1). The NFs walls display a sponge-like structure with numerous pores ranging from 2 to 4 nm, according to graphic analysis (Figure S6). Surprisingly, hollow segments within the fibers' volume were observed with bamboo-like structure. These internal cavities were observed across all Mo–SiO<sub>2</sub> NFs (Figure 1C,D and Figure S5), with the 5Mo–SiO<sub>2</sub> sample showing the highest prevalence. Wall thickness varied from 10 to 50 nm. Sample 5Mo–SiO<sub>2</sub> appeared almost hollow, emphasizing the significant presence of these cavities, as shown in Figure 1. The 7Mo–SiO<sub>2</sub> sample exhibited fewer and smaller cavities. Nonetheless, similar features were observed in all NFs prepared by this method (Figure S5). Noteworthy, significantly more complex methods based on electrospinning (i.e., coaxial electrospinning,<sup>50–52</sup> emulsion electrospinning,<sup>53–55</sup> and hard templating<sup>56–58</sup>) have been reported to obtain hollow fibers.

STEM-EDS elementals map (Figure 1, bottom) showed that silicon, oxygen, and molybdenum are distributed throughout the NFs, with no evidence of significant segregation into islands or clusters. The absence of carbon EDS signals in NFs confirmed the successful removal of PVP during the calcination step (Figure S7).

The N<sub>2</sub> adsorption–desorption isotherms of Mo–SiO<sub>2</sub> NFs, displayed in Figure 2, are type IV with hysteresis in the mesoporous region. Using the BET method, the NFs exhibited surface areas ranging from 456 to 922 m<sup>2</sup> g<sup>−1</sup>, as summarized in Table 2. Samples with 5 and 7 wt% Mo exhibited lower SSAs due to occasional imperfections observed by STEM and SEM (Figure S3). In contrary, virtually defect-free NFs 2Mo–SiO<sub>2</sub> and 11Mo–SiO<sub>2</sub> showed

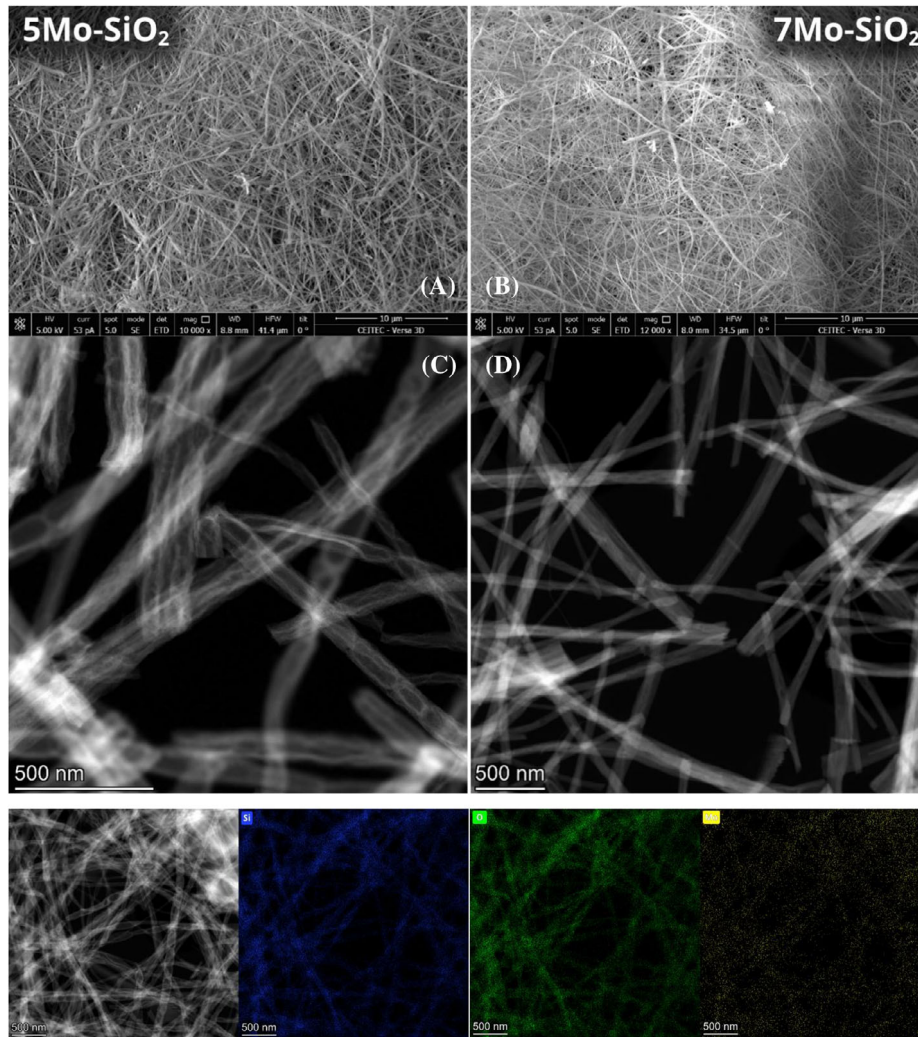


**FIGURE 1** Scanning electron microscopy (SEM) micrographs of prepared **5Mo–SiO<sub>2</sub>** (A) and **7Mo–SiO<sub>2</sub>** (B) and STEM analysis of **5Mo–SiO<sub>2</sub>** (C), and **7Mo–SiO<sub>2</sub>** (D). Elemental composition map for Si (blue), O (green), and Mo (yellow) by STEM-EDS method of sample **5Mo–SiO<sub>2</sub>** (bottom).

**TABLE 2** The specific surface area (SSA) (BET method), micropore fraction (*t*-plot method), and average pore diameter.

Sample	SSA (m <sup>2</sup> g <sup>−1</sup> )	Micropore (m <sup>2</sup> g <sup>−1</sup> )	Pore diameter <sup>a</sup> (nm)	Total pore volume (cm <sup>3</sup> g <sup>−1</sup> )	Microporous volume (cm <sup>3</sup> g <sup>−1</sup> )
2Mo–SiO <sub>2</sub>	866	465	2.5	0.544	0.204
5Mo–SiO <sub>2</sub>	456	190	3.4	0.386	0.080
7Mo–SiO <sub>2</sub>	505	343	2.3	0.287	0.135
11Mo–SiO <sub>2</sub>	922	703	2.1	0.475	0.308

<sup>a</sup>Estimated by  $d_{\text{pore}} = \frac{4 \cdot V_{\text{total}}}{\text{SA}}$ .

significantly higher and similar surface areas. No clear trend was observed between surface area changes and Mo content.

The average pore diameter of Mo–SiO<sub>2</sub> NFs ranged between 2.1 and 3.4 nm, falling within the mesoporous range (Table 2). However, a significant fraction of SSA originated from micropores, accounting for 40%–75% of the

SSA. The presence of micropores was proved by argon porosimetry (argon isotherms, pore size distributions, and SSAs are shown in Figure S8 and Table S1). Among the samples, **5Mo–SiO<sub>2</sub>** exhibited the highest mesoporous fraction, with SSA of 456 m<sup>2</sup> g<sup>−1</sup>, of which 41% originated from micropores. This sample also demonstrated the highest fraction of mesoporous volume, constituting

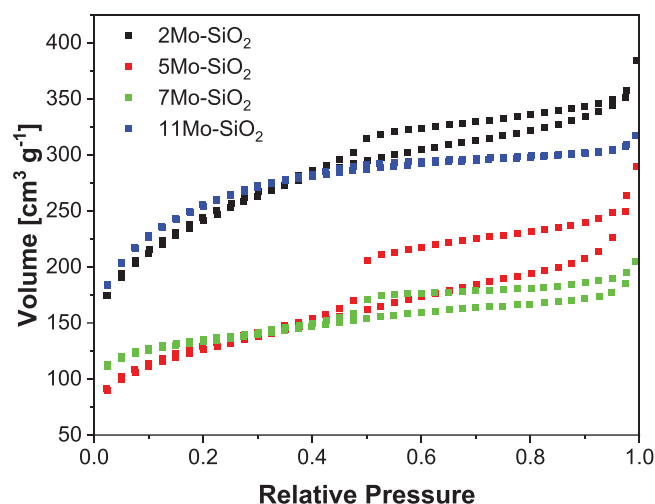


FIGURE 2 Isotherms of prepared Mo—SiO<sub>2</sub> nanofibers analyzed by N<sub>2</sub> porosimetry.

79% of its total pore volume ( $0.386 \text{ cm}^3 \text{ g}^{-1}$ ). Additionally, **2Mo—SiO<sub>2</sub>** ( $0.340 \text{ cm}^3 \text{ g}^{-1}$ ) also achieved high mesoporous pore volume (Table 2). Thus, samples with a lower Mo loading developed a higher mesoporous volume and thus generally better porosity properties, in accordance with other reports on metallosilicate materials.<sup>59</sup> All these findings underscore the structural features and potential applications of the Mo—SiO<sub>2</sub> NFs as heterogeneous catalysts, emphasizing their high surface area and mesoporous character.

XPS was used to study the surface of Mo—SiO<sub>2</sub> NFs. Particularly the Mo 3d spectra were analyzed to confirm the oxidation states of the surface MoO<sub>x</sub> species (Figure 3). Two distinct peaks were observed in the Mo 3d region corresponding to 3d 5/2 and 3d 3/2. For 5Mo—SiO<sub>2</sub>, these peaks were located at binding energies of 233.0 and 236.1 eV, respectively, whereas for 7Mo—SiO<sub>2</sub>, they appeared at 233.4 and 236.5 eV. These values are consistent with the reported binding energies of dispersed MoO<sub>x</sub> species in silica and also confirm the presence of Mo<sup>VI</sup> oxidation states in the samples.<sup>22</sup> XPS spectra of Si 2p and O 1s confirmed the presence of SiO<sub>2</sub> matrix,<sup>60–62</sup> whereas adventitious carbon<sup>63,64</sup> was detected in the C 1s region (Figure S9).

PXRD and Raman spectroscopy analyses revealed the absence of MoO<sub>3</sub> crystallization (Figures S10 and S11). No absorption bands typical for crystalline MoO<sub>3</sub><sup>65</sup> were observed at 995, 820, 666, and 286 cm<sup>−1</sup> in the Raman spectra. Accordingly, no diffraction was observed in PXRD diffractograms. Those finding was supported with HR-TEM measurement where the absence of MoO<sub>3</sub> nanoparticles and MoO<sub>x</sub> clusters was confirmed (Figures S12 and S13).

DRUV-Vis spectroscopy of the Mo—SiO<sub>2</sub> NFs revealed band edge energy ( $E_g$ ) indicative of charge transfer transitions associated with MoO<sub>x</sub> species, as shown in Figure 4. For 7Mo—SiO<sub>2</sub> NFs, the  $E_g$  value was 3.79 eV. This energy aligns more closely with well-dispersed MoO<sub>x</sub> on silica, which typically exhibits absorption bands between 3.5 and 4 eV, where clusters of polymolybdates are observed.<sup>66,67</sup> In contrast, atomically dispersed MoO<sub>x</sub> on SiO<sub>2</sub> support typically shows higher energy transitions above 4.0 eV.<sup>67,68</sup> Better distribution of MoO<sub>x</sub> species, hence likely the higher content of isolated molybdenum dioxo species, was observed for NFs with a lower molybdenum content (5Mo—SiO<sub>2</sub>).  $E_g$  was equal to 3.98 eV. Thus, 5Mo—SiO<sub>2</sub> exhibited close to atomic distribution with a small fraction of oligomerized species.<sup>69</sup> Kubelka–Munk function dependency on photon energy shown in Figure S14.

The TPR analyses provide further evidence of the high similarity of MoO<sub>x</sub> species in 5Mo—SiO<sub>2</sub> and 7Mo—SiO<sub>2</sub> samples (Figure 5). These materials exhibited broad reduction peaks at 456°C, with additional shoulders approximately at 360°C. The broad peaks indicate a variety of local environments and coordination states of the Mo atoms, consistent with the presence of non-uniformly distributed MoO<sub>x</sub> species rather than a homogeneous atomic dispersion. The shoulder at 360°C (more significant for **7Mo—SiO<sub>2</sub>**) suggests the presence of additional reducible sites, further supporting the presence of a range of catalytic centers based on MoO<sub>x</sub> species. Similar reduction temperature (456°C) was observed for **11Mo—SiO<sub>2</sub>** (Figure S15). Reduction of **2Mo—SiO<sub>2</sub>** occurred at a lower temperature (389°C). All these temperatures are significantly below the reduction temperatures reported in literature for bulk MoO<sub>3</sub> and MoO<sub>3</sub> deposited on various carbon and SiO<sub>2</sub> supports (550–900°C).<sup>70–73</sup> On the contrary, the observed TPR patterns are similar to the analyses reported for highly homogeneous MoO<sub>x</sub>—SiO<sub>2</sub> microspherical catalysts prepared by microwave-assisted sol-gel method.<sup>25</sup> Traditionally, differences in MoO<sub>x</sub> cluster size and varying interaction between MoO<sub>x</sub> species and support have been used to explain the differences in reduction temperatures.<sup>72,73</sup> More recently, strained MoO<sub>x</sub> species have been shown to undergo reduction at lower temperatures.<sup>70</sup> The increased strain might be the reason for the low reduction temperatures observed herein.

The catalytic performance of NFs was evaluated in propylene self-metathesis reaction at 200°C. The NFs were ground (Figure S16) before testing under differential conditions, free from mass and heat transfer limitations (Table S2 and Equations S1–S4). The primary products—ethylene, *cis*-2-butene, and *trans*-2-butene—were observed in a molar ratio of approximately 2:1:1, with selectivity exceeding 99% and a carbon balance over 99%. Catalysts

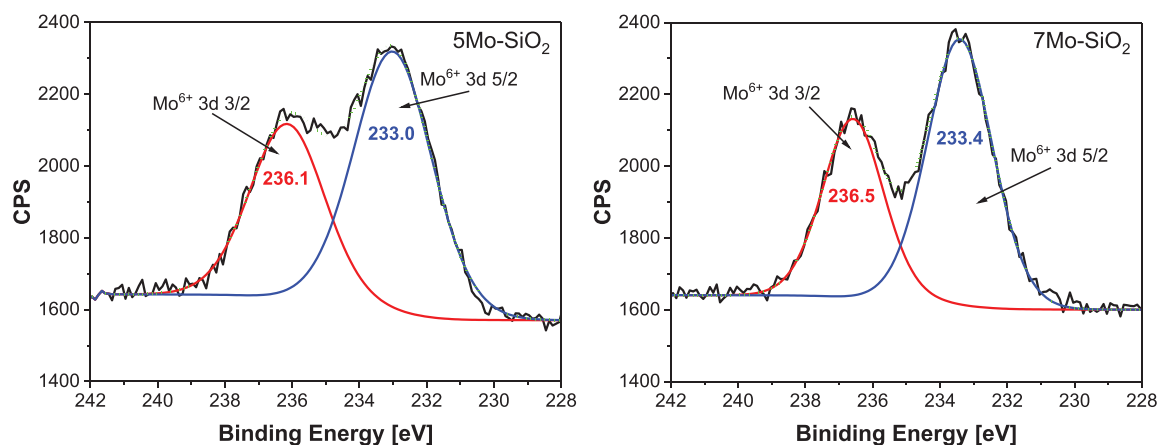


FIGURE 3 Mo 3d x-ray photoelectron spectroscopy (XPS) spectra of Mo-SiO<sub>2</sub> nanofibers.

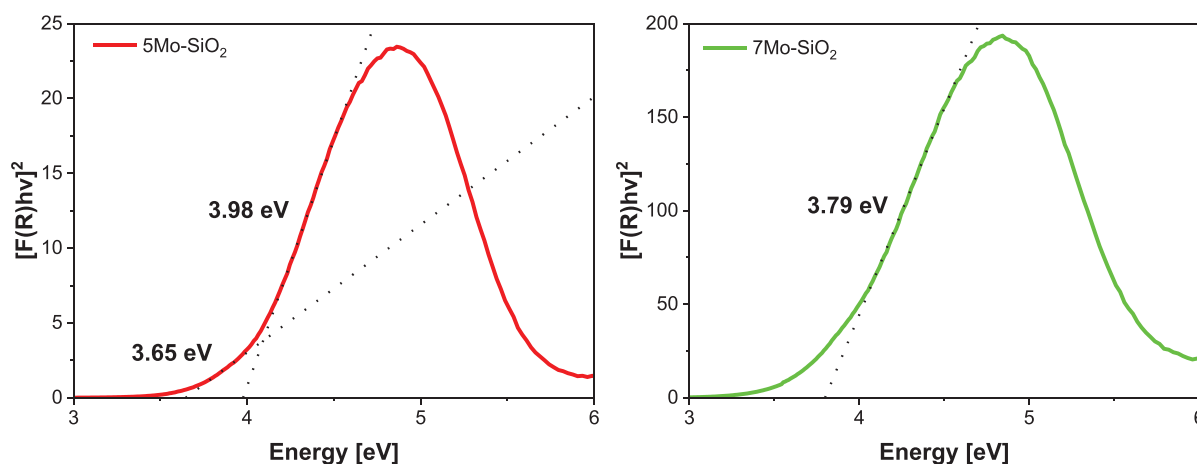


FIGURE 4 Tauc plot of energy band of Mo-SiO<sub>2</sub> nanofibers calculated by extrapolation of the linear part.

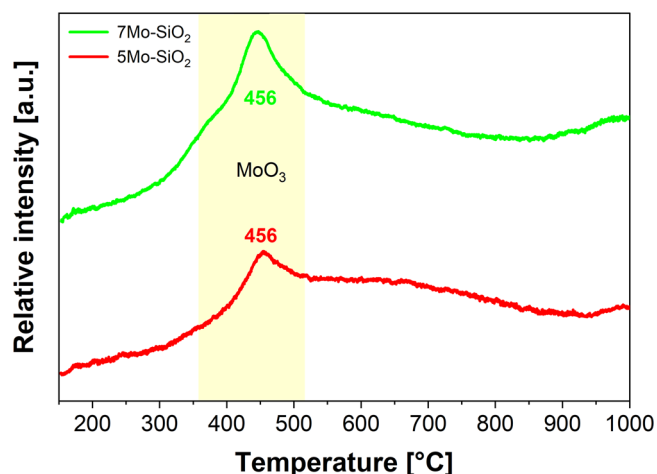


FIGURE 5 TPR analyses of 5Mo-SiO<sub>2</sub> and 7Mo-SiO<sub>2</sub> for reducibility characterization of catalytic active MoO<sub>x</sub> centers.

5Mo-SiO<sub>2</sub>, 7Mo-SiO<sub>2</sub>, and 11Mo-SiO<sub>2</sub> reached steady state after 8 h on stream.

The 5Mo-SiO<sub>2</sub> NFs exhibited a steady state rate of 17.1  $\mu\text{mol g}^{-1} \text{s}^{-1}$ , higher than the 11.1  $\mu\text{mol g}^{-1} \text{s}^{-1}$  observed for the 7Mo-SiO<sub>2</sub> NF (Figure 6, Table 3). Notably, the NFs outperformed Mo-IWI catalysts with similar Mo loading under identical reaction conditions, delivering significantly higher catalytic activity (4-MoIWI: 0.88  $\mu\text{mol g}^{-1} \text{s}^{-1}$ ; 7-MoIWI: 3.51  $\mu\text{mol g}^{-1} \text{s}^{-1}$ ).<sup>25</sup> SOMC also produced MoO<sub>x</sub>-SiO<sub>2</sub> catalyst exhibiting a lower steady state rate than NFs produced herein (1.64  $\mu\text{mol g}^{-1} \text{s}^{-1}$  for MoO<sub>x</sub>-SiO<sub>2</sub> SOMC catalyst with 1.5 wt% Mo).<sup>31</sup> The steady state rate of nanofibrous catalysts was, however, lower than the rate observed for highly homogeneous MoO<sub>x</sub>-SiO<sub>2</sub> microspherical catalysts prepared by microwave-assisted sol-gel (41.1  $\mu\text{mol g}^{-1} \text{s}^{-1}$  for MoO<sub>x</sub>-SiO<sub>2</sub> microspheres with 4 wt% Mo).<sup>25</sup> At least two important characteristics need to be considered when comparing the catalytic performance in olefin metathesis: (i) surface area (higher in nanofibrous catalysts than in chosen reported catalysts, Table 3) and (ii) band edge energy describing the MoO<sub>x</sub> species dispersion (interme-

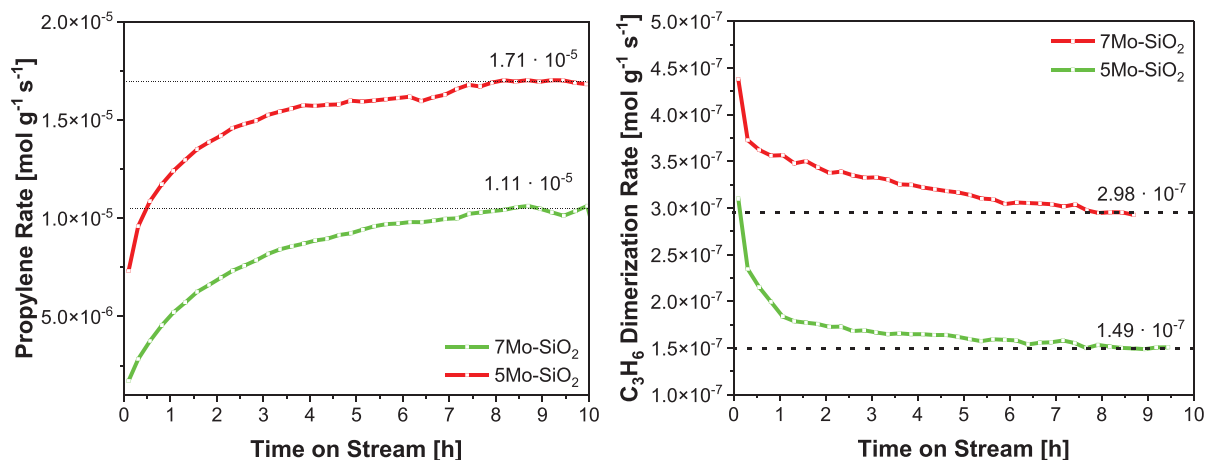


FIGURE 6 Propylene rate (left) and rate of propylene dimerization to C6 olefins (right) over 5Mo-SiO<sub>2</sub> and 7Mo-SiO<sub>2</sub> nanofibers at 200°C.

TABLE 3 Comparison of catalytic performance of MoO<sub>x</sub>-SiO<sub>2</sub> samples prepared by various synthetic methods.

Synthesis method	Mo loading (wt%)	Surface area (m <sup>2</sup> g <sup>-1</sup> )	Band edge energy (eV)	Propylene rate (μmol g <sup>-1</sup> s <sup>-1</sup> )	Dimerization rate (μmol g <sup>-1</sup> s <sup>-1</sup> )
Electrospinning	5.29	456	3.98	17.1	0.15
Electrospinning	6.99	505	3.79	11.1	0.30
Impregnation <sup>25</sup>	3.64	297	3.81	0.88	Not observed
Impregnation <sup>25</sup>	6.64	275	3.65	3.51	Not observed
MW-assisted sol-gel <sup>25</sup>	3.62	376	4.09	41.1	Not observed
SOMC <sup>31</sup>	1.5	Not studied	4.25	1.64	Not studied

diate between impregnated catalysts and MW-assisted sol-gel and SOMC prepared materials, Table 3). This results in the observed variations in catalytic activity (Table 3).

Figure S17 shows propylene rates of 2Mo-SiO<sub>2</sub> and 11Mo-SiO<sub>2</sub> catalysts. Despite its high initial activity (higher than both 5Mo-SiO<sub>2</sub> and 7Mo-SiO<sub>2</sub>), 2Mo-SiO<sub>2</sub> (2.06 wt% Mo) was not stable, exhibiting a continuous decline in activity over time on stream. In contrast, 11Mo-SiO<sub>2</sub> reached steady state. It slightly outperformed 7Mo-SiO<sub>2</sub>, maintaining a stable propylene production of 13.1 μmol g<sup>-1</sup> s<sup>-1</sup> and falling outside the observed trend (the lower the Mo loading, the higher the catalytic activity, already observed and discussed elsewhere).<sup>25</sup> However, the comparison is not entirely fair, as 11Mo-SiO<sub>2</sub> possesses a significantly higher surface area (922 m<sup>2</sup> g<sup>-1</sup>) than 7Mo-SiO<sub>2</sub> (505 m<sup>2</sup> g<sup>-1</sup>).

A promotion effect was observed for 5Mo-SiO<sub>2</sub>, with catalytic activity increasing by a factor of 1.5 when 1 mol.% of 2,3-dimethyl-butene isomers were co-fed into the reactor (Figure S18).<sup>31</sup> The promotion factors were much higher in the case of SOMC-prepared catalysts (up to 26).<sup>31</sup>

Brønsted acid-driven dimerization of propylene to C6 olefins was also observed as a minor reaction path-

way, with selectivity less than 1% for 5Mo-SiO<sub>2</sub> and 7Mo-SiO<sub>2</sub>. The C6 olefin production rate increased with Mo content, reaching 0.15 μmol g<sup>-1</sup> s<sup>-1</sup> for 5-MoSiO<sub>2</sub> and 0.30 μmol g<sup>-1</sup> s<sup>-1</sup> for 7Mo-SiO<sub>2</sub> (Figure 6). The dimerization rates at 200°C were higher for Mo-SiO<sub>2</sub> NFs than for Mo-SiO<sub>2</sub> microspheres and Mo-IWI catalysts (Table 3),<sup>25</sup> consistent with the pronounced Brønsted acidity of the NFs, as revealed by FTIR analysis of pyridine adsorption (Figure S19).

## 4 | CONCLUSION

In this study, Mo-SiO<sub>2</sub> NFs were successfully synthesized via the electrospinning method and demonstrated significant potential as heterogeneous catalysts for olefin metathesis. The NFs exhibited high surface areas (456–922 m<sup>2</sup> g<sup>-1</sup>) with favorable pore sizes (2–4 nm), contributing to their mesoporous nature and catalytic potential. PXRD, STEM-EDS, and Raman spectroscopy revealed the absence of MoO<sub>3</sub> crystallization indicating a homogeneous Mo distribution over nanofibrous samples. However, in situ DRUV-Vis spectroscopy and H<sub>2</sub>-

TPR suggested the formation of small clusters of  $\text{MoO}_x$  species.

The catalytic activity of the NFs was assessed in the self-metathesis of propylene at  $200^\circ\text{C}$ , yielding ethylene and 2-butenes with selectivity over 99% and long-term stability on stream. Notably, the  $5\text{Mo}-\text{SiO}_2$  NFs exhibited superior performance, achieving a propylene metathesis rate of  $17.1 \mu\text{mol g}^{-1} \text{s}^{-1}$ , outperforming the activity of conventional catalysts prepared by IWI. The dimerization of propylene to C6 olefins driven by Brønsted acid sites was observed as a minor reaction pathway.

## ACKNOWLEDGMENTS

The work was supported by project LUAUS23085, funded by the Ministry of Education, Youth, and Sports of the Czech Republic within the INTER-EXCELLENCE II program. We acknowledge CF CryoEM and CF NMR of CIISB, Instruct-CZ Centre, supported by MEYS CR (LM2023042) and European Regional Development Fund-Project "UP CIISB" (No. CZ.02.1.01/0.0/0.0/18\_046/0015974). Czech-NanoLab project LM2023051 funded by MEYS CR is gratefully acknowledged for the financial support of the XPS measurements at CEITEC Nano Research Infrastructure. This publication was supported by the project Quantum materials for applications in sustainable technologies (QM4ST), CZ.02.01.01/00/22\_008/0004572 by Program J. A. Comenius, call Excellent Research. The authors thank Dr. Zdenek Moravec for performing  $\text{N}_2$  and Ar adsorption-desorption analyses and Dr. Zuzana Hlavenkova for acquiring HR-TEM micrographs.

Open access publishing facilitated by Masarykova univerzita, as part of the Wiley - CzechELib agreement.


## DATA AVAILABILITY STATEMENT

Data for this article are available at Zenodo at <https://doi.org/10.5281/zenodo.15675937> (<https://doi.org/10.5281/zenodo.15675937>).

## ORCID

Tomas Pokorny  <https://orcid.org/0000-0002-6780-4738>

Ran Zhu  <https://orcid.org/0000-0003-3986-0596>

Lucie Simonikova  <https://orcid.org/0000-0003-0745-9597>

Ales Styskalik  <https://orcid.org/0000-0002-9998-6978>

Yuriy Román-Leshkov  <https://orcid.org/0000-0002-0025-4233>

David Skoda  <https://orcid.org/0000-0002-3787-1956>

## REFERENCES

- Fürstner A. Olefin metathesis and beyond. *Angew Chemie*. 2000;39(17):3012–43. [https://doi.org/10.1002/1521-3773\(20000901\)39:17<3012::AID-ANIE3012>3.3.CO;2-7](https://doi.org/10.1002/1521-3773(20000901)39:17<3012::AID-ANIE3012>3.3.CO;2-7)
- Schuster M, Blechert S. Olefin metathesis in organic chemistry. *Angew Chemie Int Ed English*. 1997;36(19):2036–56. <https://doi.org/10.1002/anie.199720361>
- Sun H, Liang Y, Thompson MP, Gianneschi NC. Degradable polymers via olefin metathesis polymerization. *Prog Polym Sci*. 2021;120:101427. <https://doi.org/10.1016/j.progpolymsci.2021.101427>
- Higman CS, Lummiss JAM, Fogg DE. Olefin metathesis at the dawn of implementation in pharmaceutical and specialty-chemicals manufacturing. *Angew Chemie Int Ed*. 2016;55(11):3552–65. <https://doi.org/10.1002/anie.201506846>
- Lin YA, Chalker JM, Davis BGO. Metathesis for site-selective protein modification. *ChemBioChem*. 2009;10(6):959–69. <https://doi.org/10.1002/cbic.200900002>
- Howell JG, Li YP, Bell AT. Propene metathesis over supported tungsten oxide catalysts: a study of active site formation. *ACS Catal*. 2016;6(11):7728–38. <https://doi.org/10.1021/acscatal.6b01842>
- Otroshchenko T, Zhang Q, Kondratenko EV. Enhancing propene formation in the metathesis of ethylene with 2-butene at close to room temperature over  $\text{MoO}_x/\text{SiO}_2$  through support promotion with P, Cl, or S. *ACS Catal*. 2021;11(22):14159–67. <https://doi.org/10.1021/acscatal.1c04267>
- Andrei AM, Bildea CS. Optimization and control of propylene production by metathesis of 2-butene. *Processes*. 2023;11(5):1325. <https://doi.org/10.3390/pr11051325>
- Mol J. Industrial applications of olefin metathesis. *Catal A Chem*. 2004;213(1):39–45. <https://doi.org/10.1016/j.molcata.2003.10.049>
- Uchagawkar A, Ramanathan A, Hu Y, Subramaniam B. Highly dispersed molybdenum containing mesoporous silicate ( $\text{Mo-TUD-1}$ ) for olefin metathesis. *Catal Today*. 2020;343:215–25. <https://doi.org/10.1016/j.cattod.2019.03.073>
- Michorczyk P, Węgrzyniak A, Węgrzynowicz A, Handzlik J. Simple and efficient way of molybdenum oxide-based catalyst activation for olefins metathesis by methane pretreatment. *ACS Catal*. 2019;9(12):11461–67. [https://doi.org/10.1021/ACSCATAL.9B03714/SUPPL\\_FILE/CS9B03714\\_SI\\_001.PDF](https://doi.org/10.1021/ACSCATAL.9B03714/SUPPL_FILE/CS9B03714_SI_001.PDF)
- Berkson ZJ, Bernhardt M, Schlapansky SL, Benedikter MJ, Buchmeiser MR, Price GA, et al. Olefin-surface interactions: a key activity parameter in silica-supported olefin metathesis catalysts. *JACS Au*. 2022;2(3):777–86. <https://doi.org/10.1021/jacsau.2c00052>
- Liu S, Li X, Xin W, Xie S, Zeng P, Zhang L, et al. Cross metathesis of butene-2 and ethene to propene over  $\text{Mo}/\text{MCM-22-Al}_2\text{O}_3$  catalysts with different  $\text{Al}_2\text{O}_3$  contents. *J Nat Gas Chem*. 2010;19(5):482–86. [https://doi.org/10.1016/S1003-9953\(09\)60095-5](https://doi.org/10.1016/S1003-9953(09)60095-5)
- Debecker DP, Stoyanova M, Rodemerck U, Léonard A, Su B-L, Gaigneaux EM. Genesis of active and inactive species during the preparation of  $\text{MoO}_3/\text{SiO}_2-\text{Al}_2\text{O}_3$  metathesis catalysts via wet impregnation. *Catal Today*. 2011;169(1):60–68. <https://doi.org/10.1016/J.CATTOD.2010.07.026>
- Hahn T, Bentrup U, Armbrüster M, Kondratenko EV, Linke D. The enhancing effect of Brønsted acidity of supported  $\text{MoO}_x$  species on their activity and selectivity in ethylene/trans -2-butene metathesis. *ChemCatChem*. 2014;6(6):1664–72. <https://doi.org/10.1002/cctc.201400040>
- Uchagawkar A, Ramanathan A, Zhu H, Chen L, Hu Y, Douglas J, et al. Insights into dopant-mediated tuning of silica-supported

- Mo metal centers for enhanced olefin metathesis. *ACS Catal.* 2024;14(11):8317–29. <https://doi.org/10.1021/acscatal.4c01700>
17. Consoli DF, Zhang S, Shaikh S, Román-Leshkov Y. Influence of framework heteroatoms on olefin metathesis activity using MoO<sub>3</sub>-MFI catalysts. *Org Process Res Dev.* 2018;22(12):1683–86. [https://doi.org/10.1021/ACS.OPRD.8B00336/SUPPL\\_FILE/OP8B00336\\_SI\\_001.PDF](https://doi.org/10.1021/ACS.OPRD.8B00336/SUPPL_FILE/OP8B00336_SI_001.PDF)
  18. Gholampour N, Yusubov M, Verpoort F. Investigation of the preparation and catalytic activity of supported Mo, W, and Re oxides as heterogeneous catalysts in olefin metathesis. *Catal Rev.* 2016;58(1):113–56. <https://doi.org/10.1080/01614940.2015.1100871>
  19. Copéret C, Berkson ZJ, Chan KW, de J, Silva J, Gordon CP, et al. Olefin metathesis: what have we learned about homogeneous and heterogeneous catalysts from surface organometallic chemistry? *Chem Sci.* 2021;12(9):3092–115. <https://doi.org/10.1039/D0SC06880B>
  20. Lwin S, Wachs IE. Olefin metathesis by supported metal oxide catalysts. *ACS Catal.* 2014;4(8):2505–20. <https://doi.org/10.1021/cs500528h>
  21. Debecker DP, Schimmoeller B, Stoyanova M, Poleunis C, Bertrand P, Rodemerck U, et al. Flame-made MoO<sub>3</sub>/SiO<sub>2</sub>-Al<sub>2</sub>O<sub>3</sub> metathesis catalysts with highly dispersed and highly active molybdate species. *J Catal.* 2011;277(2):154–63. <https://doi.org/10.1016/j.jcat.2010.11.003>
  22. Skoda D, Hanulíková B, Styskalík A, Vykoukal V, Machac P, Urbanek P, et al. Non-aqueous synthesis of homogeneous molybdenum silicate microspheres and their application as heterogeneous catalysts in olefin epoxidation and selective aniline oxidation. *J Ind Eng Chem.* 2022;107:320–32. <https://doi.org/10.1016/j.jiec.2021.12.001>
  23. Debecker DP, Bouchmella K, Stoyanova M, Rodemerck U, Gaigneaux EM, Hubert Mutin P. A non-hydrolytic sol–gel route to highly active MoO<sub>3</sub>-SiO<sub>2</sub>-Al<sub>2</sub>O<sub>3</sub> metathesis catalysts. *Catal Sci Technol.* 2012;2(6):1157. <https://doi.org/10.1039/c2cy00475e>
  24. Debecker DP, Bouchmella K, Poleunis C, Eloy P, Bertrand P, Gaigneaux EM, et al. Design of SiO<sub>2</sub>-Al<sub>2</sub>O<sub>3</sub>-MoO<sub>3</sub> metathesis catalysts by nonhydrolytic sol–gel. *Chem Mater.* 2009;21(13):2817–24. <https://doi.org/10.1021/cm900490t>
  25. Skoda D, Zhu R, Hanulíková B, Styskalík A, Vykoukal V, Machac P, et al. Propylene metathesis over molybdenum silicate microspheres with dispersed active sites. *ACS Catal.* 2023;13(19):12970–82. <https://doi.org/10.1021/acscatal.3c02045>
  26. Debecker DP, Stoyanova M, Colbeau-Justin F, Rodemerck U, Boissière C, Gaigneaux EM, et al. One-pot aerosol route to MoO<sub>3</sub>-SiO<sub>2</sub>-Al<sub>2</sub>O<sub>3</sub> catalysts with ordered super microporosity and high olefin metathesis activity. *Angew Chemie Int Ed.* 2012;51(9):2129–31. <https://doi.org/10.1002/anie.201106277>
  27. Wang J, Li X, Zhang S, Lu R. Facile synthesis of ultrasmall monodisperse “raisin–bun”-type MoO<sub>3</sub>/SiO<sub>2</sub> nanocomposites with enhanced catalytic properties. *Nanoscale.* 2013;5(11):4823. <https://doi.org/10.1039/c3nr01097j>
  28. Poater A, Solans-Monfort X, Clot E, Copéret C, Eisenstein O. Understanding of olefin metathesis catalysts: which metal, which ligands? *J Am Chem Soc.* 2007;129(26):8207–16. <https://doi.org/10.1021/ja070625y>
  29. Berkson ZJ, Zhu R, Ehinger C, Lätsch L, Schmid SP, Nater D, et al. Active site descriptors from 95 Mo NMR signatures of silica-supported Mo-based olefin metathesis catalysts. *J Am Chem Soc.* 2023;145(23):12651–62. <https://doi.org/10.1021/jacs.3c02201>
  30. Amakawa K, Wrabetz S, Kröhnert J, Tzolova-Müller G, Schlögl R, Trunschke AI. Situ generation of active sites in Olefin metathesis. *J Am Chem Soc.* 2012;134(28):11462–73. <https://doi.org/10.1021/ja3011989>
  31. Gani TZH, Berkson ZJ, Zhu R, Kang JH, Di Iorio JR, Chan KW, et al. Promoting active site renewal in heterogeneous olefin metathesis catalysts. *Nature.* 2023;617(7961):524–28. <https://doi.org/10.1038/s41586-023-05897-w>
  32. Maksasithorn S, Praserttham P, Suriye K, Debecker DP. Preparation of super-microporous WO<sub>3</sub>-SiO<sub>2</sub> olefin metathesis catalysts by the aerosol-assisted sol–gel process. *Microporous Mesoporous Mater.* 2015;213:125–33. <https://doi.org/10.1016/j.micromeso.2015.04.020>
  33. Debecker DP. Innovative sol–gel routes for the bottom-up preparation of heterogeneous catalysts. *Chem Rec.* 2018;18(7–8):662–75. <https://doi.org/10.1002/tcr.201700068>
  34. Vass P, Szabó E, Domokos A, Hirsch E, Galata D, Farkas B, et al. Scale-up of electrospinning technology: applications in the pharmaceutical industry. *WIREs Nanomed Nanobi.* 2020;12(4):e1611. <https://doi.org/10.1002/wnan.1611>
  35. Xuyen NT, Ra EJ, Geng H-Z, Kim KK, An KH, Lee YH. Enhancement of conductivity by diameter control of polyimide-based electrospun carbon nanofibers. *J Phys Chem B.* 2007;111(39):11350–53. <https://doi.org/10.1021/jp075541q>
  36. Koo JY, Hwang S, Ahn M, Choi M, Byun D, Lee W. Controlling the diameter of electrospun yttria-stabilized Zirconia nanofibers. *J Am Ceram Soc.* 2016;99(9):3146–50. <https://doi.org/10.1111/jace.14331>
  37. Mirtič J, Balažić H, Zupančič Š, Kristl J. Effect of solution composition variables on electrospun alginate nanofibers: response surface analysis. *Polymers (Basel).* 2019;11(4):692. <https://doi.org/10.3390/polym11040692>
  38. Anis SF, Khalil A, Saepurahman, Singaravel G, Hashaikh R. A review on the fabrication of zeolite and mesoporous inorganic nanofibers formation for catalytic applications. *Microporous Mesoporous Mater.* 2016;236:176–92. <https://doi.org/10.1016/j.micromeso.2016.08.043>
  39. Liu Y, He J, Yu J, Zeng H. Controlling numbers and sizes of beads in electrospun nanofibers. *Polym Int.* 2008;57(4):632–36. <https://doi.org/10.1002/pi.2387>
  40. Khajavi R, Abbasipour M. Controlling nanofiber morphology by the electrospinning process. In: *Electrospun nanofibers*. Amsterdam: Elsevier; 2017. <https://doi.org/10.1016/B978-0-08-100907-9.00005-2>
  41. Li L, Peng S, Lee JKY, Ji D, Srinivasan M, Ramakrishna S. Electrospun hollow nanofibers for advanced secondary batteries. *Nano Energy.* 2017;39:111–39. <https://doi.org/10.1016/j.nanoen.2017.06.050>
  42. Xue J, Xie J, Liu W, Xia YEN. New concepts, materials, and applications. *Acc Chem Res.* 2017;50(8):1976–87. <https://doi.org/10.1021/acs.accounts.7b00218>
  43. Li M, Loccufier E, Geltmeyer J, Vandevyvere T, Singh VJ, Sabbe M, et al. One-step electrospinning of alumina nanofibers to create a competitive esterification catalyst. *J Am Ceram Soc.* 2025;108:e70007. <https://doi.org/10.1111/JACE.70007>
  44. Loccufier E, Debecker DP, D’hooge DR, De Buysser K, De Clerck K. Fibrous material structure developments for sustain-

- able heterogeneous catalysis—an overview. *ChemCatChem*. 2024;16:e202301563. <https://doi.org/10.1002/cctc.202301563>
45. Zhu R, Adamji H, Berkson Z, Zhu J, Head A, Kulik H, et al. Insights into the catalytic promotion of propylene self-metathesis over silica-supported molybdenum oxide using substituted olefins. *ChemRxiv*. May 8, 2024. <https://doi.org/10.26434/chemrxiv-2024-f7dh4>
  46. Schneider CA, Rasband WS, Eliceiri KW. NIH image to ImageJ: 25 years of image analysis. *Nat Methods*. 2012;9(7):671–75. <https://doi.org/10.1038/nmeth.2089>
  47. Choi S, Lee SG, Im SS, Kim SH, Joo YL. Silica nanofibers from electrospinning/sol-gel process. *J Mater Sci Lett*. 2003;22(12):891–93. <https://doi.org/10.1023/a:1024475022937>
  48. Patel AC, Li S, Wang C, Zhang W, Wei Y. Electrospinning of porous silica nanofibers containing silver nanoparticles for catalytic applications. *Chem Mater*. 2007;19(6):1231–38. <https://doi.org/10.1021/cm061331z>
  49. Zhao Y, Wang H, Lu X, Li X, Yang Y, Wang C. Fabrication of refining mesoporous silica nanofibers via electrospinning. *Mater Lett*. 2008;62(1):143–46. <https://doi.org/10.1016/j.matlet.2007.04.096>
  50. Li D, McCann JT, Xia Y. Use of electrospinning to directly fabricate hollow nanofibers with functionalized inner and outer surfaces. *Small*. 2005;1(1):83–86. <https://doi.org/10.1002/sml.200400056>
  51. Chen H, Wang N, Di J, Zhao Y, Song Y, Jiang L. Nanowire-in-microtube structured core/shell fibers via multifluidic coaxial electrospinning. *Langmuir*. 2010;26(13):11291–96. <https://doi.org/10.1021/la100611f>
  52. Liu Y, Ma Q, Yang M, Dong X, Yang Y, Wang J, et al. Flexible hollow nanofibers: novel one-pot electrospinning construction, structure and tunable luminescence-electricity-magnetism trifunctionality. *Chem Eng J*. 2016;284:831–40. <https://doi.org/10.1016/j.cej.2015.09.030>
  53. Yarin AL. Coaxial electrospinning and emulsion electrospinning of core-shell fibers. *Polym Adv Technol*. 2011;22(3):310–17. <https://doi.org/10.1002/pat.1781>
  54. Bazilevsky AV, Yarin AL, Megaridis CM. Co-electrospinning of core-shell fibers using a single-nozzle technique. *Langmuir*. 2007;23(5):2311–14. <https://doi.org/10.1021/la063194q>
  55. Yu Y, Gu L, Zhu C, van Aken PA, Maier J. Tin nanoparticles encapsulated in porous multichannel carbon microtubes: preparation by single-nozzle electrospinning and application as anode material for high-performance Li-based batteries. *J Am Chem Soc*. 2009;131(44):15984–85. <https://doi.org/10.1021/ja906261c>
  56. Choi SW, Park JY, Lee C, Lee JG, Kim SS. Synthesis of highly crystalline hollow TiO<sub>2</sub> fibers using atomic layer deposition on polymer templates. *J Am Ceram Soc*. 2011;94(7):1974–77. <https://doi.org/10.1111/j.1551-2916.2011.04600.x>
  57. Yan C, Chen G, Zhou X, Sun J, Lv C. Template-based engineering of carbon-doped Co<sub>3</sub>O<sub>4</sub> hollow nanofibers as anode materials for lithium-ion batteries. *Adv Funct Mater*. 2016;26(9):1428–36. <https://doi.org/10.1002/adfm.201504695>
  58. Yoo J, Kim J, Jung YS, Kang K. Scalable fabrication of silicon nanotubes and their application to energy storage. *Adv Mater*. 2012;24(40):5452–56. <https://doi.org/10.1002/adma.201201601>
  59. Styskalik A, Kordoghli I, Poleunis C, Delcorte A, Moravec Z, Simonikova L, et al. Hybrid mesoporous aluminosilicate catalysts obtained by non-hydrolytic sol-gel for ethanol dehydration. *J Mater Chem A*. 2020;8(44):23526–42. <https://doi.org/10.1039/D0TA07016E>
  60. Pokorny T, Vykoukal V, Machac P, Moravec Z, Scotti N, Roupceva P, et al. Ethanol dehydrogenation over copper-silica catalysts: from sub-nanometer clusters to 15 nm large particles. *ACS Sustain Chem Eng*. 2023;11(30):10980–92. <https://doi.org/10.1021/acssuschemeng.2c06777>
  61. Pokorny T, Doroshenko I, Machac P, Simonikova L, Bittova M, Moravec Z, et al. Copper phosphinate complexes as molecular precursors for ethanol dehydrogenation catalysts. *Inorg Chem*. 2023;62(49):19871–86. <https://doi.org/10.1021/acs.inorgchem.3c01678>
  62. Mitchell DF, Clark KB, Bardwell JA, Lennard WN, Massoumi GR, Mitchell IV. Film thickness measurements of SiO<sub>2</sub> by XPS. *Surf Interface Anal*. 1994;21(1):44–50. <https://doi.org/10.1002/sia.740210107>
  63. Barr TL, Seal S. Nature of the use of adventitious carbon as a binding energy standard. *J Vac Sci Technol A Vacuum, Surfaces, Film*. 1995;13(3):1239–46. <https://doi.org/10.1116/1.579868>
  64. Greczynski G, Hultman L. C 1s peak of adventitious carbon aligns to the vacuum level: dire consequences for material's bonding assignment by photoelectron spectroscopy. *ChemPhysChem*. 2017;18(12):1507–12. <https://doi.org/10.1002/cphc.201700126>
  65. Kothaplamoottil Sivan S, Padinjareveetil AKK, Padil VVT, Pilankatta R, George B, Senan C, et al. Greener assembling of MoO<sub>3</sub> nanoparticles supported on gum arabic: cytotoxic effects and catalytic efficacy towards reduction of p-nitrophenol. *Clean Technol Environ Policy*. 2019;21(8):1549–61. <https://doi.org/10.1007/s10098-019-01726-9>
  66. Lee EL, Wachs IE. Situ spectroscopic investigation of the molecular and electronic structures of SiO<sub>2</sub> supported surface metal oxides. *J Phys Chem C*. 2007;111(39):14410–25. <https://doi.org/10.1021/jp0735482>
  67. Tian H, Roberts CA, Wachs IE. Molecular structural determination of molybdena in different environments: aqueous solutions, bulk mixed oxides, and supported MoO<sub>3</sub> catalysts. *J Phys Chem C*. 2010;114(33):14110–20. <https://doi.org/10.1021/jp103269w>
  68. Zhang B, Ford ME, Ream E, Wachs IE. Olefin metathesis over supported MoO<sub>x</sub> catalysts: influence of the oxide support. *Catal Sci Technol*. 2022;13(1):217–25. <https://doi.org/10.1039/d2cy01612e>
  69. Miyata N, Suzuki T, Ohyama R. Physical properties of evaporated molybdenum oxide films. *Thin Solid Films*. 1996;281–282(1–2):218–22. [https://doi.org/10.1016/0040-6090\(96\)08617-8](https://doi.org/10.1016/0040-6090(96)08617-8)
  70. Amakawa K, Sun L, Guo C, Hävecker M, Kube P, Wachs IE, et al. How strain affects the reactivity of surface metal oxide catalysts. *Angew Chemie Int Ed*. 2013;52(51):13553–57. <https://doi.org/10.1002/anie.201306620>
  71. Song Z, Mimura N, Bravo-Suárez JJ, Akita T, Tsubota S, Oyama ST. Gas-phase epoxidation of propylene through radicals generated by silica-supported molybdenum oxide. *Appl Catal A Gen*. 2007;316(2):142–51. <https://doi.org/10.1016/j.apcata.2006.08.029>
  72. Rajagopal S, Marini HJ, Marzari JA, Miranda R. Silica-alumina-supported acidic molybdenum catalysts—TPR and XRD characterization. *J Catal*. 1994;147(2):417–28. <https://doi.org/10.1006/jcat.1994.1159>
  73. Feng L, Li X, Dadyburjor DB, Kugler EL. A temperature-programmed-reduction study on alkali-promoted,

carbon-supported molybdenum catalysts. *J Catal.* 2000;190(1): 1–13. <https://doi.org/10.1006/jcat.1999.2744>

## SUPPORTING INFORMATION

Additional supporting information can be found online in the Supporting Information section at the end of this article.

**How to cite this article:** Pokorny T, Zhu R, Simonikova L, Styskalik A, Román-Leshkov Y, Skoda D. Electrospun Mo—SiO<sub>2</sub> nanofibers as heterogeneous catalysts for propylene metathesis. *J Am Ceram Soc.* 2026;109:e70339. <https://doi.org/10.1111/jace.70339>